A posteriori Synchronization of Scanning Transmission Electron Microscopy Signals with Kilopixel Per Second Acquisition Rates

Tobias Meyer,[*,†] Sergei Lopatin,[‡] Michael Seibt,[†] and Vladimir Roddatis[¶]

†*4th Institute of Physics -– Solids and Nanostructures, University of Goettingen, Friedrich-Hund-Platz 1, 37077 Göttingen, Germany*

‡*King Abdullah University of Science and Technology (KAUST), Core Labs, Thuwal, 23955-6900, Saudi Arabia*

¶*Institute of Materials Physics, University of Goettingen, Friedrich-Hund-Platz 1, 37077 Göttingen, Germany*

E-mail: tmeyer@uni-goettingen.de

Abstract

The stability and sensitivity of scanning transmission electron microscopes as well as detectors collecting e.g. electrons which suffered different scattering processes, or secondary radiation, have increased tremendously during the last decade. In order to fully exploit capabilities of simultaneously recording various signals with up to 1000 px/s acquisition rates the central issue is their synchronization. The latter is frequently a non-trivial problem without commercially available solution especially if detectors of different manufacturers are involved. In this paper, we present a simple scanning pattern enabling *a posteriori* synchronization of arbitrarily many signals being recorded entirely independently. We apply the approach to the simultaneous atomic-scale acquisition of signals from an annular dark-field detector and electron energy loss as well

as energy-dispersive x-ray spectrometers. Errors emerging in scanning direction due to the independence of the respective processes are quantified and found to have a standard deviation of roughly half the pixel spacing. Since there are no intermediate waiting periods to maintain synchronicity, the proposed acquisition process is, in fact, demonstrated to be 12% faster than a commercial hardware-synchronized solution for identical sub-millisecond signal integration times and hence follows the trend in electron microscopy to extract more information per irradiating electron.

Keywords: STEM; Synchronization; EELS; EDX; 4DSTEM

Introduction

Scanning transmission electron microscopy (STEM) offers a vast variety of signals which can be recorded simultaneously.[1] Besides the detection of electrons being scattered in a certain angular range, analytical methods like electron energy-loss spectroscopy (EELS) and energy-dispersive X-ray spectroscopy (EDX)[2,3] are commonly used in order to determine the chemical composition of materials. However, synchronizing the acquisition of signals with the scanning movement of the focused electron beam can be challenging, especially since recent progress in detection and lens systems technology, enabling high-speed data collection with sub Å spatial resolution,[4–6] demands for synchronicity at kilopixel per second scanning speeds .

In this work, we introduce an experimental scheme which completely separates data acquisition and synchronization. More explicitly, data sets from various sources are recorded independently, i.e. without any hardware synchronization. This type of data acquisition will subsequently be referred to as *'streaming mode'*. For *a posteriori* synchronization, marker signals are included into the acquisition at specific previously defined points. As an example, we use a script as described in the following section to move the beam to a position in vacuum after each completed scanning line. Subsequently, the beginning and end of each scanning line can be identified in the acquired data by the marker enabling for a spatial reconstruction.

The concept is shown to be applicable to kilopixel per second data collection. Since there are no waiting periods to maintain hardware synchronicity during the acquisition, faster data collection can be realized, i.e. a ratio of acquisition time and life time close to one.

Although the quality of *a posteriori* synchronized data is comparable to that of traditionally recorded data, some inherent error sources can be identified as being due to the missing phase lock, different clocking periods as well as clocking irregularities of different recording devices. These errors are described quantitatively and confirmed by a comparison to images resulting from hardware-synchronized data.

Experimental Procedure

Sample Preparation and Microscopy Parameters

An electron transparent $SrTiO_3$ (STO) foil has been extracted from a commercial substrate employing an FEI Nova NanoLab Dual Beam focused ion beam. During mounting on the support grid, the stage was tilted to 20° guaranteeing a coinciding decrease of X-ray shielding with the zone axis alignment in the STEM. All data has been collected in an FEI Titan 80-300 operated at 300 kV and equipped with a Gatan Quantum 965 ER image filter as well as a stand-alone Oxford Instruments X-Max 80 mm^2 EDX detector. The energy ranges for the chemical analysis of EELS and EDX data are summarized in table 1. Additionally, a Keithley DMM6500 digital multimeter has been used to continuously read out the output voltage of the Gatan annular dark field (ADF) detector included in the image filter which is proportional to the electron current impinging on the detector. The inner and outer diameter of the detector are 4.3 mm and 24 mm, respectively. Throughout all experiments the beam current was set to 100 pA and the camera length was chosen to be 38 mm resulting in an acceptance semi-angle of the spectrometer of 39 mrad and an inner and outer collection semi-angle of the ADF detector of 46.8 mrad and 200 mrad.

Table 1: Chosen energy windows for EELS background fitting, EELS Ti L-edge integration after background subtraction as well as all EDX edges.

	E_{min} [eV]	E_{min} [eV]
EELS background	384	448
EELS Ti L-edge	451	515
EDX Sr L-edge	1,709	1,989
EDX Ti K-edge	4,362	5,069
EDX Sr K-edge	13,856	16,237

Data Acquisition and Reconstruction

The beam movements in streaming mode have been controlled by a custom Gatan Digital Micrograph (DM) script employing a Gatan DigiScan II scan unit. Image reconstructions were performed using custom DM scripts as well. All scripts are available in the supplementary material.[7] A sketch of the post-acquisition reconstruction procedure is given in figure 1: After the marker signal is localized in the continuous readout of the detector (a) the lines are arranged (b). Due to irregularities in the acquisition or scanning speed the length of the lines might differ slightly hence they are scaled (c) and interpolated (d) to the desired amount of scanning positions per line.

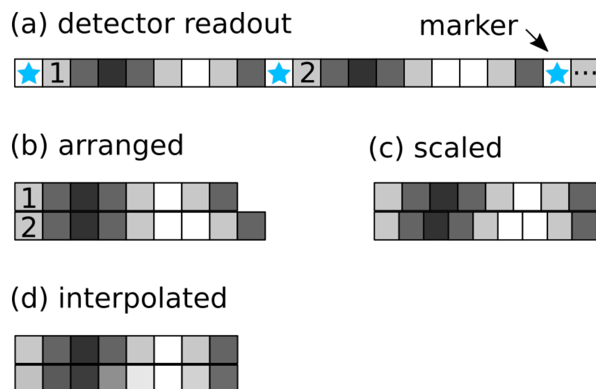

Figure 1: Sketch of the image reconstruction. The continuous readout of the detector (a) is, according to the marker positions, arranged line by line (b) and subsequently scaled (c) and interpolated (d) to the amount of desired scanning positions.

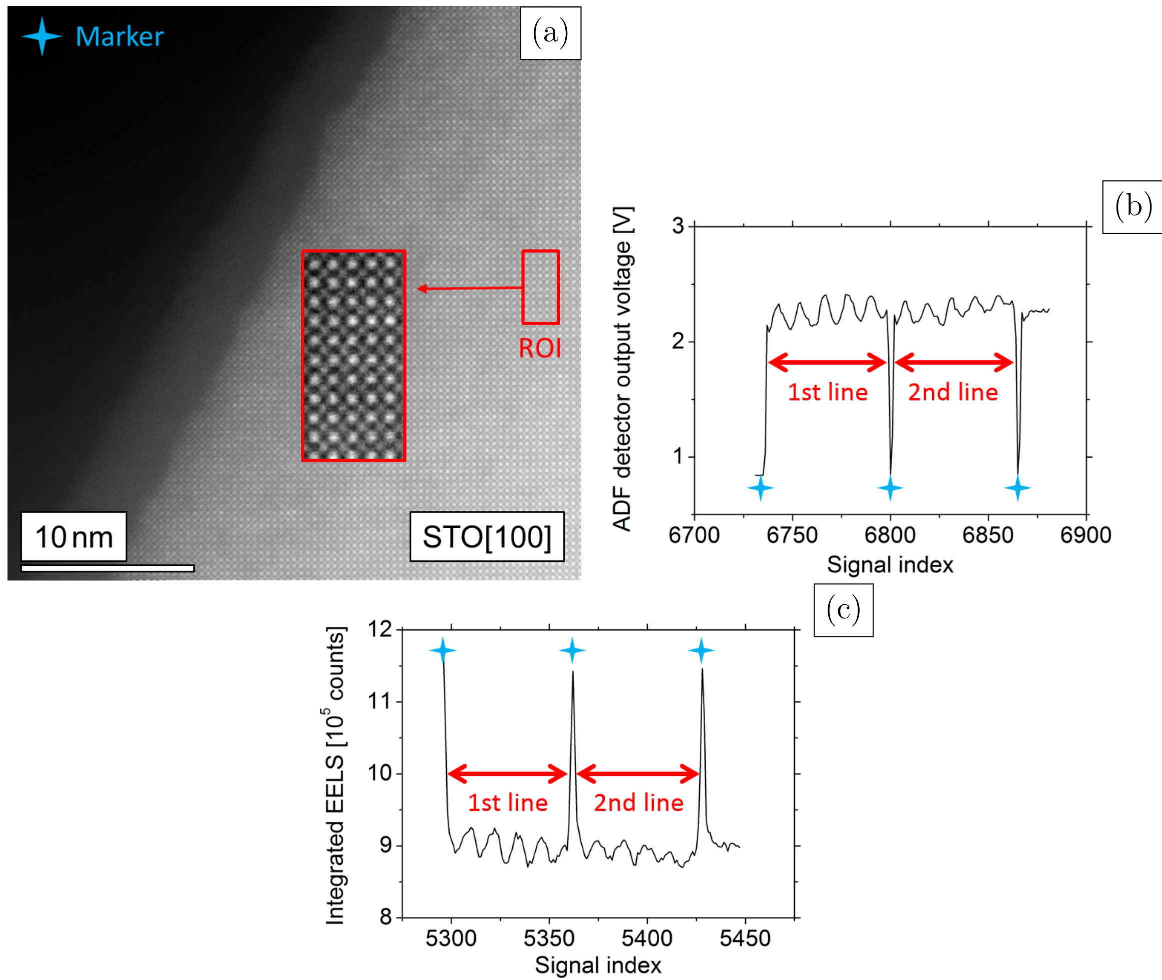

Figure 2: Overview ADF-STEM image of the [100] oriented STO lamella including the 64 by 128 pixels ROI and the vacuum marker position which are scanned with 1000 px/s acquisition rate (a) as well as excerpts of the simultaneously collected ADF detector output voltage (b) and integrated EELS spectra (c).

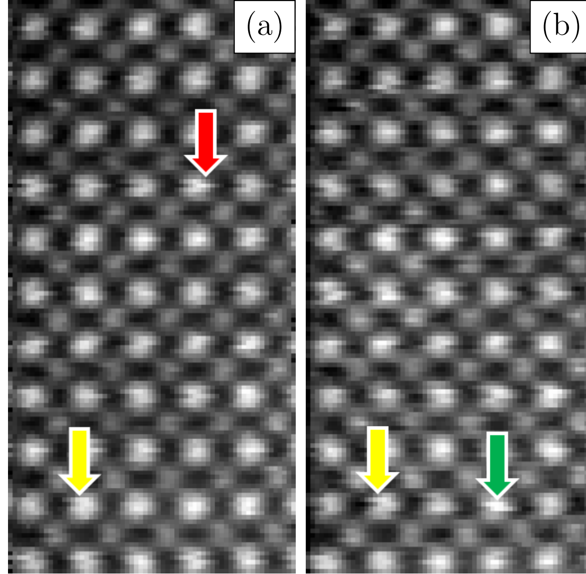

Figure 3: *A posteriori* reconstructed ADF (a) and inverted integrated EELS (b) signal corresponding to the reference in figure 2. Exemplary artifacts emerging only in the ADF signal (red), only in the EELS signal (green) and which coincide (yellow) are marked with arrows.

Results and Discussion

In this section, two exemplary combinations of signals will be elaborated. Firstly, ADF as well as low-loss EELS signals collected with 1000 px/s acquisition rates will be compared to prove that the suggested scanning pattern is applicable to high-speed data collection and to quantify resulting errors. Secondly, a lower acquisition rate of 10 px/s is chosen to include the possibility of EDX spectra collection in order to emphasize the high methodology's versatility.

High-Speed Data Acquisition

Figure 2 (a) shows an ADF overview image (acquired in standard STEM mode) of [100] oriented STO including the scanned region of interest (ROI) as well as the vacuum marker position of the first example. The total acquisition time for 64 by 128 pixels inside the ROI and an acquisition rate of 1000 px/s was 8.3 s. Additionally, excerpts of the ADF detector output voltage and the integrated EELS spectra are given in (b) and (c), respectively, in or-

der to illustrate typical signals obtained in streaming mode. Note that the entrance aperture of the spectrometer limits the scattering angle of the collected electrons hence the integrated EELS spectra mimic a bright field signal. The blue stars in both line profiles clearly indicate the vacuum marker position such that the signals in between can be attributed to the corresponding lines of the ROI. More technically, each point is assigned to be in vacuum if the signal is lower than 1.5 V or greater than 10.5×10^5 counts for ADF and EELS, respectively.

Following the reconstruction procedure mentioned before leads to figure 3 (a) and (b). For the sake of comparison, the integrated EELS signal has been inverted in order to mimic a dark field signal. As marked by the colored arrows, flag-like artifacts can either coincide or appear in only one the signals. Whereas the latter is a strong hint for acquisition rate instabilities of the respective detectors, the former could be both explained by irregularities of the beam movement clocking as well as general instabilities of the microscope leading to commonly observed distortions in STEM images.[8] Notwithstanding these occasional flaws, it can be concluded that *a posteriori* synchronized images are of comparable quality of hardware-synchronized data sets as will be demonstrated below.

In order to compare the method to state of the art commercial products, the hardware-synchronized Gatan Spectrum Imaging (SI) tool has been used to obtain the data shown in figure 4. Clearly, it is less likely to find flags in the hardware-synchronized images and those that appear seem to coincide in both signals as marked by the yellow arrows hence one cannot directly relate the artifacts to clocking instabilities.

Error Quantification

Since the eye-guided search for artifacts in the images is rather qualitative and highly subjective, a more thorough error estimation will be given in this subsection. First, we note that resolution and accuracy in the vertical direction is determined by the microscope and does not suffer from *a posteriori* synchronization. The horizontal direction, however, is affected due to the accidental inclusion of signals from different scanning points during one

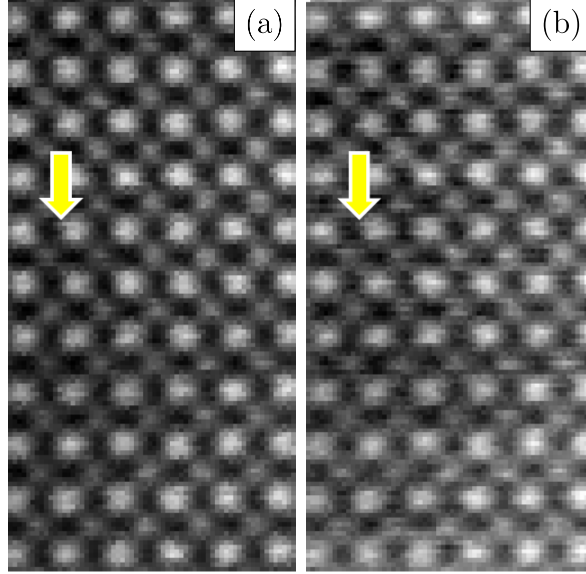

Figure 4: ADF (a) and inverted integrated EELS (b) signal close to the reference in figure 2 obtained with the hardware-synchronized Gatan SI tool. A coinciding artifact is marked with yellow arrows.

acquisition. Three independent sources of experimental uncertainty can be identified, i.e. (i) the missing phase lock (experimental uncertainty σ_{ph}), (ii) a possible difference in the mean clocking periods of different recording devices (σ_{per}), and (iii) irregularities in their clocking processes (σ_{irr}). The total experimental uncertainty σ can then be written as

$$\sigma = \sqrt{\sigma_{\mathrm{ph.}}^2 + \sigma_{\mathrm{per.}}^2 + \sigma_{\mathrm{irr.}}^2}\,.$$

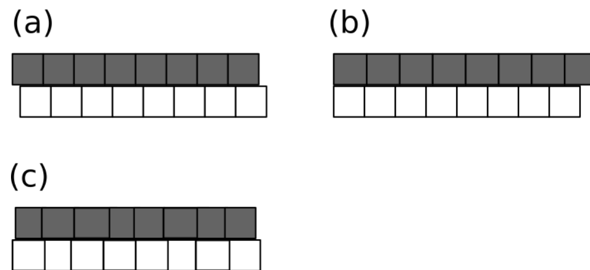

Figure 5: Visualization of the synchronization error sources: The grey and white boxes represent beam dwelling and signal integration periods. (a) shows a constant offset due to the missing phase lock, (b) an increasing delay due to different mean clocking periods, and (c) a stochastic scattering of the respective periods due to irregularities.

A graphical illustration of the error sources is given in figure 5, where grey boxes refer to the dwelling periods of the beam and white boxes signal integration periods. Firstly, the missing phase lock leads to a uniformly distributed spread between 50% with the previous and 50% with the next pixel hence the standard deviation of the resulting error is given by that of the uniform distribution within the interval $[-0.5, 0.5]$ times the pixel spacing Δx, i.e. $\sigma_{\text{ph.}} = \Delta x/\sqrt{12}$. Secondly, the maximum spread with neighboring points within a line due to different mean clocking periods is given by the number of scanning points N per line times the relative difference of the periods. Estimating the latter with $|\overline{N}_{\text{acq.}} - N|/N$, where $N_{\text{acq.}}$ is the averaged number of acquisitions per line, leads to $\sigma_{\text{per.}} = \Delta x \cdot |\overline{N}_{\text{acq.}} - N|$. Finally, the irregularities in the clocking processes can be estimated by the standard deviation of the acquisitions per line times the pixel spacing $\sigma_{\text{irr.}} = \Delta x \cdot \sigma_{N_{\text{acq.}}}/\sqrt{2}$. Note that the division by $\sqrt{2}$ accounts for the fact that both the irregularities of the first and the last pixel contribute equally to the fluctuation in $N_{\text{acq.}}$. It is worth mentioning that $\sigma_{\text{ph.}}$ represents the theoretical limit of the proposed method for perfectly regular and coherent clocking processes and therefore the margin to a perfect time synchronization. For the sake of quantification, five acquisitions have been performed analogously to the one shown in figure 3 yielding the averaged error contributions in table 2.

Table 2: Error contributions of the missing phase lock $\sigma_{\text{ph.}}$, different mean clocking periods $\sigma_{\text{per.}}$, and clocking irregularities $\sigma_{\text{irr.}}$ to the total error σ of the *a posteriori* synchronization of ADF and EELS signals.

	ADF	EELS
$\sigma_{\text{ph.}}$ $[\Delta x]$	0.29	0.29
$\sigma_{\text{per.}}$ $[\Delta x]$	0.27	0.28
$\sigma_{\text{irr.}}$ $[\Delta x]$	0.3	0.32
σ $[\Delta x]$	0.49	0.52

A second and rather experimental approach to assess the error resulting from *a posteriori* synchronization is to compare the data to hardware-synchronized acquisitions quantitatively. Due to the similarity of the inverted integrated EELS and ADF signals, a high Cross-Correlation Coefficient (CCC) of the reconstructed images is expected. Note that the

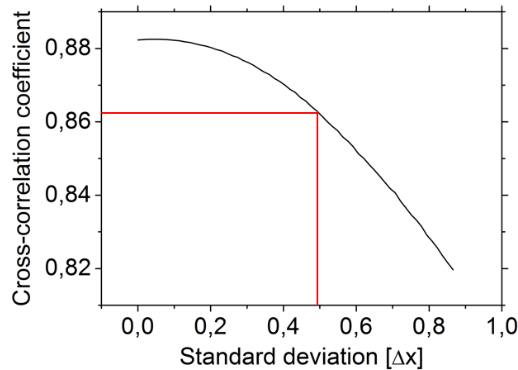

Figure 6: Cross-correlation coefficient (averaged over 100 runs) of hardware-synchronized ADF and inverted integrated EELS images with respect to the standard deviation of a uniformly distributed shift in the EELS sampling position. The signals of non-integer shifted sampling positions have been interpolated with next neighbors. The red lines mark the point at which the initial value is reduced by 0.02.

first and last pixels of each line have been omitted in the following calculations since they contain strongly deviating signal from the marker position. In fact, this reduces the fraction of useful data in the *a posteriori* synchronized images to 96.9% which will be taken into account later in the conclusion. To maintain equal conditions, the same omission has been performed to hardware-synchronized data as well. The mean CCC of the reduced *a posteriori* synchronized images obtained by five acquisitions is 0.867(12). Using Gatan SI, a slightly higher value of 0.886(8) could be achieved with an average acquisition time of 9.6 s. The reduction of CCC caused by asynchronicities can be modeled by shifting the horizontal sampling points in one of the hardware-synchronized EELS images according to a random variable. Due to its similarity to a missing phase lock, a uniform distribution around the initial sampling point has been used. The signals of non-integer shifted sampling positions have been interpolated with next neighbors. For each fixed standard deviation of the distribution the CCC between the shifted EELS and unaltered ADF images has been averaged over 100 runs to reduce probabilistic scattering and can be found in figure 6. In remarkable consistence with the values of table 2, the margin of 0.02 in the CCC can be resembled with a standard deviation of roughly 0.49 Δx as marked by the red lines.

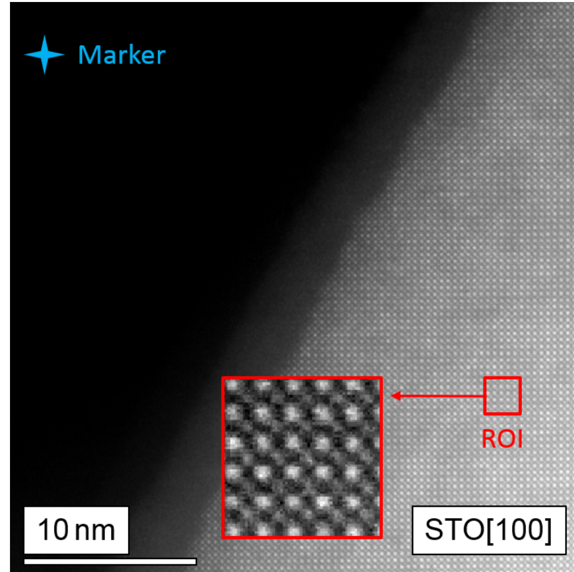

Figure 7: Overview ADF-STEM image of the [100] oriented STO lamella including the 32 by 32 pixels ROI and the vacuum marker position which are scanned with 10 px/s acquisition rate.

The Method's Versatility

In order to demonstrate how easily a third signal acquisition can be included, the acquisition rate was reduced to 10 px/s to achieve an acceptable EDX signal-to-noise ratio. Scanning the ROI shown in figure 7 with 32 by 32 pixels results in a total acquisition time of 102 s. The localization of the marker signal in the ADF and EELS signal was done analogously to the first example whereas for EDX the Cu K-edge counts related to the support grid on which the lamella was mounted were used. Once the correlation between signal index and spatial position has been obtained, any analysis, e.g. chemical mapping, can be performed. Figure 8 shows the reconstructed ADF signal (a) as well as a map of the integrated EELS Ti L-edge obtained after power law background subtraction (b), the integrated EDX Sr K- and L-edge (d) and the integrated EDX Ti-K edge (e). Even though the statistics of the EDX map is still poor compared to ADF and EELS and the effect of small drift is apparent, the atomic structure of STO is clearly visible in all images. As the superimposed color images in figure 8 (c) and (f) with Ti contributions in red illustrate, consistent chemical contrast is achieved combining the ADF signal with EELS respectively the two EDX edges. Given the

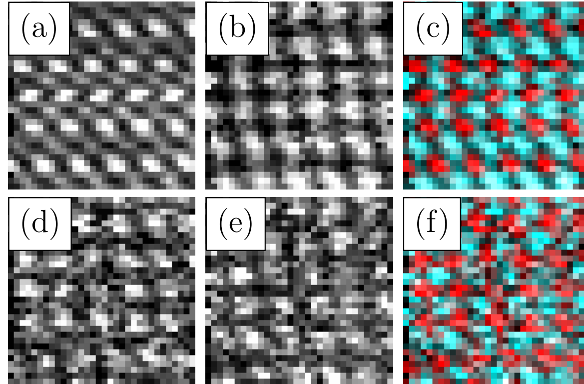

Figure 8: *A posteriori* reconstructed signals corresponding to the reference in figure 7: ADF signal (a), integrated EELS Ti-L edge after background subtraction (b), sum of EDX Sr K- and L-edge (d) and EDX Ti K-edge (e) counts. Details about the respective energy windows are given in table 1. (c) shows a superimposed color image with (b) in red and (a) in cyan. (f) shows a superimposed color image with (e) in red and (d) in cyan.

lower scanning rate, the predominant distortion of the images is caused by sample drift.

Summary and Conclusion

We have presented a scanning pattern allowing for *a posteriori* synchronization of STEM data by marking the end of each line with a distinct signal of a marker position. Images of simultaneously collected ADF detector voltages and EELS spectra have been reconstructed yielding atomic resolution for acquisition rates up to 1000 px/s evidencing the applicability to modern fast digital cameras.

Comparison with Hardware Synchronization

Compared to hardware-synchronized setups, the method causes an additional spread in scanning direction which is in theory at least $1/\sqrt{12}$ times and in practice roughly 0.5 times the pixel spacing. Notwithstanding this limitation, *a posteriori* synchronization adds value to existing solutions in terms of speed: As mentioned in the previous section, the acquisition of a 64 by 128 pixels frame with an acquisition rate of 1000 px/s took 8.3 s. In order to achieve such a high EELS readout rate, the exposure time was set to 440 µs. Using the

same exposure time and experimental conditions with the Gatan SI tool results in a total acquisition time of 9.6 s. After accounting for the omission of the first and last pixels in the *a posteriori* images this corresponds to a speed gain of 12% and hence the detection of more signal per incoming electron. Particularly in the field of beam sensitive materials, the resulting reduction of electron dose can be very advantageous. In addition, the ordering of the scanning lines could be changed with an ease or even probed in a sparse sampling approach like it has been presented before.[9]

The Method's Versatility

Furthermore, the high versatility of the method has been proven by collecting and synchronizing EDX spectra in addition, i.e. we collected signals which could not be combined in our setup before. In fact, in the second example, data of three sources was collected using two independently running computers and the direct read-out of the multimeter. Consequently, detectors of different manufacturers running on different platforms can be combined without any constraints.

One possible application that we would like to emphasize at this point is the collection of entire diffraction patterns for each scanning position also referred to as 4DSTEM. Since the diffraction patterns contain a large variety of information this approach can be used to map physical quantities such as electric or magnetic fields as well as strain.[10–13] The popularity of 4DSTEM has raised tremendously due to the improvement of digital cameras, i.e. direct detectors are capable of recording several thousand diffraction patterns per second – an acquisition rate to which the presented method has proven to be applicable.

Conditions and Limitations

The only necessary conditions are the possibility to control the electron beam as well as the availability of a marker position exhibiting a distinct signal. The latter can consist of only one point as in the examples shown here, but allows also for some creative workarounds

such as using a more complicated template similar to a Morse code or choosing a marker that occurs only in the center of lines and exploiting the knowledge of the approximate amount of signals per line to locate its beginning and end. Another possible solution to the non-existence of a distinct area is to use the electron beam to drill a hole in the sample which we have successfully tested. Still, in the case of a low signal to noise ratio, the exact localization of the marker sequence might become difficult leading to additional distortions in the reconstructed images.

The effect of sample drift becomes apparent using small acquisition rates as shown in figure 8. The robustness of the method against this depends on the localization of the marker sequence, i.e. if the signals of the latter change significantly due to small sample movements the reconstruction can be difficult. On the other hand, assuming that the signal evolution of the marker sequence under translation is known, one could even use this effect to correct for sample drift.

In conclusion, we have described and implemented a simple but powerful *a posteriori* synchronization scheme which can be considered as a trade-off between higher speed and flexibility on the upside and lower spatial resolution in scanning direction on the downside: The method allows for simultaneous device-independent recording of arbitrarily many signals during STEM acquisitions with up to 1000 px/s and offers, in the regime of small integration times, a speed gain of 12%. The spatial blurring in scanning direction was quantified to be only half a pixel spacing.

Acknowledgments

We thank Christian Jooss and the anonymous reviewers sincerely for carefully reading the manuscript and helping to improve its quality. Funding by the Deutsche Forschungsgemeinschaft (DFG) via the CRC 1073, project B02 and Z02, is gratefully acknowledged.

Author Contributions

The original idea was conceived by S.L and V.R.: The design of experiments was the result of fruitful discussions including all authors; T.M. conducted the measurements and wrote the DM script with advise of V.R.; M.S. and V.R. supervised the study. The manuscript was written by T.M. under revision of S.L., M.S. and V.R.; All authors read and agreed on the written paper.

Conflicts of Interest

Conflicts of Interest: The authors declare no conflict of interest.

References

(1) Crewe, A. The physics of the high-resolution scanning microscope. *Reports on Progress in Physics* **1980**, *43*, 621.

(2) Isaacson, M.; Johnson, D. The microanalysis of light elements using transmitted energy loss electrons. *Ultramicroscopy* **1975**, *1*, 33–52.

(3) Lyman, C.; Williams, D.; Goldstein, J. X-ray detectors and spectrometers. *Ultramicroscopy* **1989**, *28*, 137–149.

(4) Kirkland, E. J. Fine tuning an aberration corrected ADF-STEM. *Ultramicroscopy* **2018**, *186*, 62–65.

(5) Milazzo, A.-C.; Moldovan, G.; Lanman, J.; Jin, L.; Bouwer, J. C.; Klienfelder, S.; Peltier, S. T.; Ellisman, M. H.; Kirkland, A. I.; Xuong, N.-H. Characterization of a direct detection device imaging camera for transmission electron microscopy. *Ultramicroscopy* **2010**, *110*, 741–744.

(6) Krajnak, M.; McGrouther, D.; Maneuski, D.; O'Shea, V.; McVitie, S. Pixelated detectors and improved efficiency for magnetic imaging in STEM differential phase contrast. *Ultramicroscopy* **2016**, *165*, 42–50.

(7) Meyer, T.; Lopatin, S.; Seibt, M.; Roddatis, V. Supplementary Material. *Ultramicroscopy*

(8) Ning, S.; Fujita, T.; Nie, A.; Wang, Z.; Xu, X.; Chen, J.; Chen, M.; Yao, S.; Zhang, T.-Y. Scanning distortion correction in STEM images. *Ultramicroscopy* **2018**, *184*, 274 – 283.

(9) Kovarik, L.; Stevens, A.; Liyu, A.; Browning, N. D. Implementing an accurate and rapid sparse sampling approach for low-dose atomic resolution STEM imaging. *Applied Physics Letters* **2016**, *109*, 164102.

(10) Müller, K.; Krause, F. F.; Béché, A.; Schowalter, M.; Galioit, V.; Löffler, S.; Verbeeck, J.; Zweck, J.; Schattschneider, P.; Rosenauer, A. Atomic electric fields revealed by a quantum mechanical approach to electron picodiffraction. *Nature communications* **2014**, *5*, 5653.

(11) Lopatin, S.; Ivanov, Y. P.; Kosel, J.; Chuvilin, A. Multiscale differential phase contrast analysis with a unitary detector. *Ultramicroscopy* **2016**, *162*, 74–81.

(12) Cooper, D.; Denneulin, T.; Bernier, N.; Béché, A.; Rouvière, J.-L. Strain mapping of semiconductor specimens with nm-scale resolution in a transmission electron microscope. *Micron* **2016**, *80*, 145–165.

(13) Gammer, C.; Ophus, C.; Pekin, T. C.; Eckert, J.; Minor, A. M. Local nanoscale strain mapping of a metallic glass during in situ testing. *Applied Physics Letters* **2018**, *112*, 171905.